ACS APPLIED ENERGY MATERIALS

www.acsaem.org Article

Selective Thermophotovoltaic Emitter with Aperiodic Multilayer Structures Designed by Machine Learning

Wenbin Zhang, Boxiang Wang, and Changying Zhao*

Cite This: *ACS Appl. Energy Mater.* 2021, 4, 2004–2013 Read Online

ACCESS | Metrics & More | Article Recommendations | Supporting Information

ABSTRACT: Controlling the thermal emission characteristics of a thermophotovoltaic (TPV) emitter can effectively reduce the thermal losses in a photovoltaic cell. Moreover, selective TPV emitters can facilitate the generation of electricity from a variety of high-temperature waste heat sources. To overcome the challenge of achieving perfect spectral selectivity of TPV emitters, the development of artificial intelligence provides a vision for the optimization of selective TPV emitters beyond the conventional paradigm. In this work, we demonstrate that a highly selective, aperiodic TPV emitter with a high figure of merit (FOM) can be achieved with the help of Bayesian optimization. The design of the selective TPV emitter is optimized over 5.23×10^9 candidate structures in multilayers consisting of multiple components to maximize the FOM. The maximum FOM could be realized within calculations for less than 0.67% of the total candidate structures, which is much better than other machine learning algorithms. As for the gallium antimonide photovoltaic cell, the resulting optimal structure is an aperiodic multilayer structure with an FOM of 82.16%. The optimal structure is then fabricated by a multi-target sputtering system, and the experimental result of the emission characteristics is achieved with an FOM of 81.35%, which is significantly better than those of multilayers with similar material designed and fabricated based on previous studies. What is more, we have analyzed the efficiency of the TPV system and measured the thermal stability of the fabricated samples. The results demonstrate that Bayesian optimization is efficient in designing selective TPV emitters, and the machine-learning-based design of metamaterials can be extended for the expensive black-box global optimization problems in other field applications.

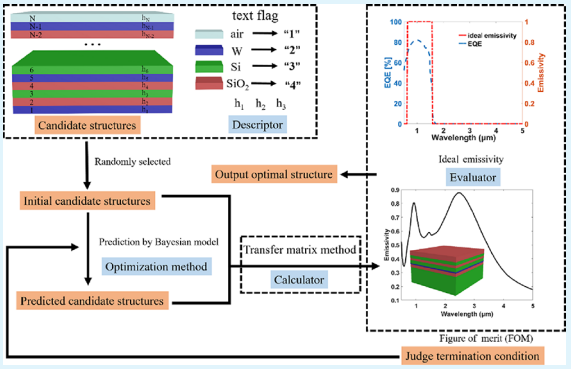

KEYWORDS: *machine learning algorithm, selective TPV emitter, Bayesian optimization, aperiodic multilayer metamaterials, thermal stability*

1. INTRODUCTION

A large amount of wasted energy in the world is discharged into the environment every day in the form of cooling water,[1] hot exhaust gases,[2] and thermal losses from thermal equipment.[3,4] Recycling and utilizing this waste heat energy is important for improving the energy efficiency and reducing global warming.[3,5] At present, one of the effective solutions for this aim is thermophotovoltaic (TPV) systems,[6] for example, waste heat recovery in high temperature industries such as melting processing.[7] In a TPV system, photons are radiated from a thermal emitter and received by a photovoltaic (PV) cell and then photons are converted into electrical energy by the photoelectric effect.[8−10] What is more, various kinds of heat sources can be used for TPV systems. Controlling the thermal emission characteristics of a TPV emitter can effectively reduce the thermal losses in a photovoltaic cell, in principle leading to a TPV system with an efficiency greater than the Shockley−Queisser limit.[11,12] Also, the system efficiency can be further improved by employing the near-field TPV systems[13−15] due to the near-field effects.[16−18] However, despite many decades of research, the TPV system efficiencies of existing TPV systems remain far lower than the theoretical maximum because of the challenge of achieving perfect spectral selectivity of TPV emitters.[19]

In the design of selective TPV emitters, a knotty problem that researchers usually face is to decide the choices of desired materials and structural parameters.[20] In practice, selective TPV emitters are usually fabricated as simple periodic structures, although in fact these periodic structures are a very small fraction of the set of possible multilayer structures.[21−23] Only a few studies have reported the regulation of the emissivity of thermal emitters by aperiodic multilayer structures,[24,25] and the design of aperiodic structures

Received: December 23, 2020
Accepted: January 25, 2021
Published: February 3, 2021

https://dx.doi.org/10.1021/acsaem.0c03201
ACS Appl. Energy Mater. 2021, 4, 2004–2013

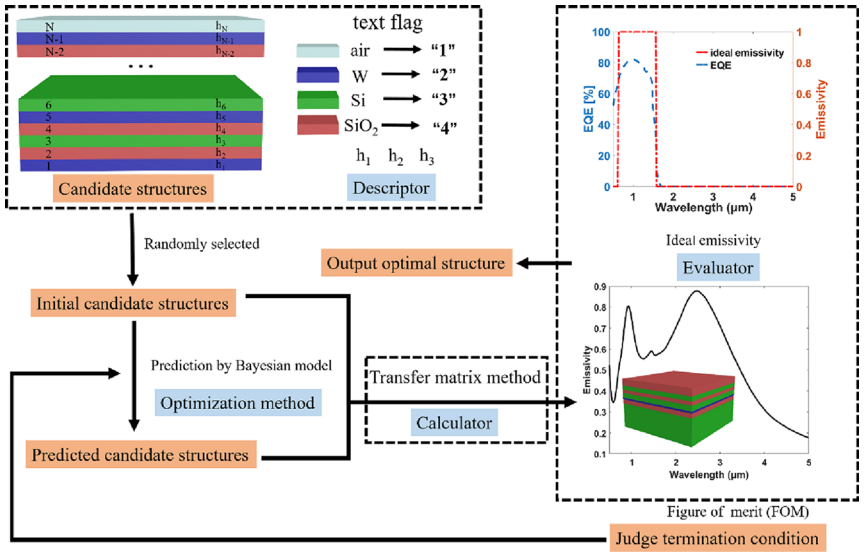

Figure 1. Flowchart for design optimization of the selective TPV emitter. The EQE of the GaSb PV cell and the ideal emission spectrum for the GaSb PV cell of the TPV system is in the upper right corner.

with the expected emission spectrum is highly demanding because the number of possible candidate multilayer structures is enormous. However, the development of artificial intelligence[26] provides a new concept for the optimization of selective TPV emitters beyond the strictly theoretical approach.[27,28] A variety of machine learning algorithms have been described in the literature to design thermal emitters,[29] such as genetic algorithms,[30] adversarial autoencoder network,[31] and particle swarm optimization.[32] However, these methods usually require large data sets of evaluation samples over the objective function, either time-consuming calculations or expensive experiments. Moreover, the main disadvantage of these methods is that they are "exploitation only". It should be noted that methods that balance exploitation and exploration are more efficient than exploitation only methods.[33] Recently, Bayesian optimization[34,35] has attracted attention as a method to accelerate the design of the desired metamaterials. By making use of Bayesian inference to quantify uncertainties, the Bayesian optimization method achieves the best balance between exploration and exploitation.[36,37] Bayesian optimization is successfully applied in the metamaterial design, for instance, designing ultranarrow-band thermal emission with metamaterials through the Bayesian optimization method.[38]

In this work, we employ the Bayesian optimization method to design the highly wavelength-selective, aperiodic multilayer TPV emitters. Based on the combination of the Bayesian optimization method and the transfer matrix method (TMM), the selective TPV emitter is optimized over 5.23×10^9 candidate structures to maximize the figure of merit (FOM). As for the gallium antimonide (GaSb) PV cell, the optimal structure of aperiodic multilayers consists of silicon (Si), silica (SiO_2), and tungsten (W) with the global maximum FOM, which is 82.16%. The optimal structure is fabricated by an automatic multi-target sputtering system; then, we measure the emission spectrum to compare with the predicted emission spectrum. What is more, the thermal stability of the selective TPV emitters at high operating temperatures is an important factor for the TPV system; thus, we measure the emission spectrum of the fabricated samples after heating at different temperatures and for different times. This is the first time that the Bayesian optimization algorithm is used to design an efficient selective TPV emitter. Our approach shows that Bayesian optimization is powerful in designing multilayer structures for other applications.

2. THEORY AND METHODS

In this section, we introduce how the Bayesian optimization approach is applied to design an aperiodic multilayer selective TPV emitter. First of all, let us discuss the ideal emission spectrum for selective TPV emitters. The current availability of high-quality, low-band gap PV cells are from the III−V family of compound semiconductors and alloys.[39] PV cells made of GaSb are widely used in TPV systems.[40,41] It is mainly due to the fact that the GaSb PV cells have excellent external quantum efficiency (EQE) at infrared wavelengths and therefore does not require the operation of the TPV system at extremely high temperatures. In the case of a GaSb PV cell at $T = 300$ K, the band gap energy is about 0.726 eV,[42] the corresponding band gap wavelength is 1.708 μm. The top right corner in Figure 1 shows the EQE of the GaSb PV cell[43] and the ideal emission spectrum for selective TPV emitters. It means that the ideal selective TPV emitter has high emissivity for wavelengths (0.6−1.708 μm) shorter than the band gap wavelength of the PV cell and minimizes emissivity otherwise.

Figure 1 displays the flowchart for design optimization of the selective TPV emitter. The structure of the selective TPV emitter is divided into N unit layers with different thicknesses h. Each unit layer can be either W, Si, or SiO_2. These structural component materials are easy to process and frequently used materials for their high melting point, making them excellent for high-temperature TPV emitters. And W is highly lossy in the visible and near-infrared wavelengths, which can enhance the emissivity at the target wavelength region. The optimization process is mainly composed of four parts: a descriptor, an evaluator, a calculator, and an optimization method.

The descriptor is mainly used to describe possible candidate structures in the optimization process. In the optimization process, we employ the text flag to represent each material: "1", "2", "3", and "4" represent the air, W, Si, and SiO_2, respectively, and the value of thickness of each layer can be used directly in the Bayesian optimization.

The ideal selective TPV emitter has high thermal emissivity at the target wavelength region and low thermal emissivity in the other wavelength region, as illustrated in Figure 1. For the evaluator of the desired emission spectrum of the selective TPV emitter, an FOM can be defined as follows:[44]

https://dx.doi.org/10.1021/acsaem.0c03201
ACS Appl. Energy Mater. 2021, 4, 2004−2013

$$\mathrm{FOM} = \frac{\int_{\lambda_1}^{\lambda_{pv}} \varepsilon_\lambda E_{b\lambda} d\lambda}{\int_{\lambda_1}^{\lambda_{pv}} E_{b\lambda} d\lambda} - \frac{\int_{\lambda_{pv}}^{\lambda_2} \varepsilon_\lambda E_{b\lambda} d\lambda}{\int_{\lambda_{pv}}^{\lambda_2} E_{b\lambda} d\lambda} - \frac{\int_{\lambda_0}^{\lambda_1} \varepsilon_\lambda E_{b\lambda} d\lambda}{\int_{\lambda_0}^{\lambda_1} E_{b\lambda} d\lambda} \quad (1)$$

where $E_{b\lambda}$ indicates the spectral blackbody intensity. ε_λ denotes the spectral normal emissivity. λ_0 and λ_2 are the minimum and maximum wavelengths considered for this optimization process. In this work, we assume that λ_0 = 0.5 μm and λ_2 = 5 μm. λ_{pv} is the band gap wavelength of the GaSb PV cell. According to Planck's law, when the operating temperature of the selective TPV emitter is below 2000 K, we find that the emissive intensity of the blackbody below the λ_1 = 0.6 μm is little; thus, we can minimize emissivity between 0.5 μm and 0.6 μm.

As shown in the equation of FOM, in order to calculate the spectral normal emissivity, we employ the TMM.[45] In the TMM, the field amplitude of each layer can be calculated by its relative permittivity, and the total transfer matrix connects the field amplitude of different layers, which can be written as:[46]

$$\begin{pmatrix} M_{11} & M_{12} \\ M_{21} & M_{22} \end{pmatrix} = \left[\prod_{n=0}^{N-2} V_{n,n+1} P_{n,n+1}\right] V_{N-1,N}, \quad (2)$$

where the transmission matrix $V_{n,n+1} = \frac{1}{t_{n,n+1}} \begin{bmatrix} 1 & r_{n,n+1} \\ r_{n,n+1} & 1 \end{bmatrix}$ refers to the amplitudes of the waves at the interface s of layer n and layer n + 1, $t_{n,n+1}$ and $r_{n,n+1}$ denote Fresnel's transmission and reflection coefficients, respectively. The propagation matrix of layer n can be given by $P_{n,n+1} = \begin{bmatrix} e^{-ik_z d_n} & 0 \\ 0 & e^{ik_z d_n} \end{bmatrix}$, and the reflectivity can be obtained by $R_\lambda = \left(\frac{M_{21}}{M_{11}}\right)^2$. The dielectric functions of Si, SiO_2, and W are obtained from the handbook of optical constants.[47] The spectral directional emission spectrum can be obtained by employing Kirchhoff's law, i.e., $\varepsilon_\lambda = 1 - R_\lambda$, where R_λ is the reflectivity obtained from the TMM. Therefore, enhancing the emissivity of a multilayer structure is equivalent to minimizing reflectivity because the transmission and scattering are so small.

As for the optimization method, Bayesian optimization is an active optimization method. An open-source package (COMmon Bayesian Optimization)[48] is used throughout the optimization process. The framework of the Bayesian optimization mainly contains two core parts: the probabilistic surrogate model and the acquisition function.[49] The probabilistic surrogate model is mainly used for surrogating unknown functions. The model starts from an a priori hypothesis, iteratively increases the amount of prior information, and modifies the prior model to obtain a more accurate surrogate model. The probabilistic model in this optimization is a Gaussian process. Gaussian processes use a prior over functions, which can incorporate prior beliefs about the objective function. On the other hand, we use the acquisition function to propose the next sampling point. The acquisition function in this optimization is based on an upper confidence bound. In the optimization process, the scikit-learn model is used for the Gaussian processes and Python modules (NumPy and SciPy) are used to implement the acquisition function.

3. RESULTS AND DISCUSSIONS

3.1. Performance of Bayesian Optimization. In this work, the temperature of the selective emitter in the optimization process is 1200 K. First, we calculated the candidate structures with different number of layers or different thicknesses (10, 30, 50, 70, and 90 nm) by Bayesian optimization or traversal calculation, as illustrated in Figure 2. We can find that when the number of layers is 10, further increase in the number of layers does not increase the maximum FOM. It explains that the optimal selective TPV emitters can be obtained in less than 10 unit layers. Therefore, we think n = 10 is enough to optimize the selective TPV emitter. Note that the air can be only on the top layer, so the number of possible candidate structures with the same thickness of each layer is 88,572 rather than 4^{10}, and the best thickness in the structures is between 50 and 70 nm. Therefore, we plan that the thickness of each layer has three different choices (45, 55, and 65 nm), and the number of possible candidate structures is 88,572 × 3^{10} = 5,230,147,077. The computational load is too heavy to calculate all of the candidate structures in one round. In order to reduce the computational load, the optimization process is calculated step by step. The overall candidate structures are randomly divided into 10,000 groups. First, we optimize each group and then rank these 10,000 local best FOMs to find the optimal structure of all candidate structures. The weakness of the approach of grouping is that the computational time becomes relatively large, because Bayesian optimization should be performed in each group.

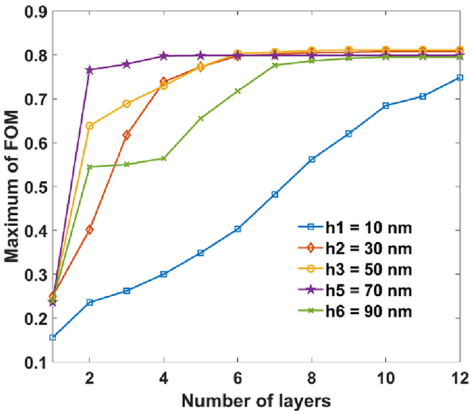

Figure 2. Maximum FOM with different numbers of layers or different thicknesses.

For verifying the performance of the Bayesian optimization method, we calculate different rounds of optimization. Figure 3a,b display the search histories of the FOM with the number of calculated structures for different groups and the same group with different random seeds, respectively. As shown in Figure 3b, our chosen group of candidate structures includes the global optimized structure. Figure S1a,b show the number of calculated candidate structures needed to find the optimal FOM for different groups and the same group with different random seeds, respectively. We can find that all the rounds of optimization converged to the maximum FOM by calculating less than 3500 candidate structures, which indicates that only 0.67% of the candidate structures needed to be evaluated to identify the optimal structure. This demonstrates that Bayesian optimization is much better than other machine learning algorithms for designing of the selective TPV emitters.[50]

Through Bayesian optimization, the maximum FOM of the selective TPV emitter can be found, which is 82.16%, and the text flag of the optimal selective TPV emitter is "2 2 2 2 3 2 3 4 4 1" and the flag of thickness is "55 65 65 55 55 45 55 45 55 45". The inset of Figure 3b shows the sketch map of the optimal structure, we can see that the materials of the best selective TPV emitter are SiO_2/Si/W/Si/W from the top to the bottom, and the thickness of each layer is 100, 55, 45, 55, and 240 nm from the top to the bottom. The total thickness of the aperiodic multilayer is 495 nm. Note that the structure of

https://dx.doi.org/10.1021/acsaem.0c03201
ACS Appl. Energy Mater. 2021, 4, 2004−2013

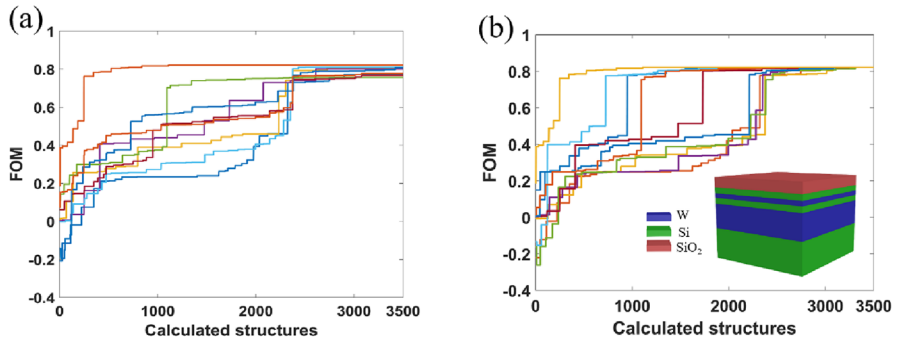

Figure 3. Histories of the FOM with respect to the number of calculated structures during the 10 random optimization rounds for (a) different groups and (b) same group with different random seeds, respectively.

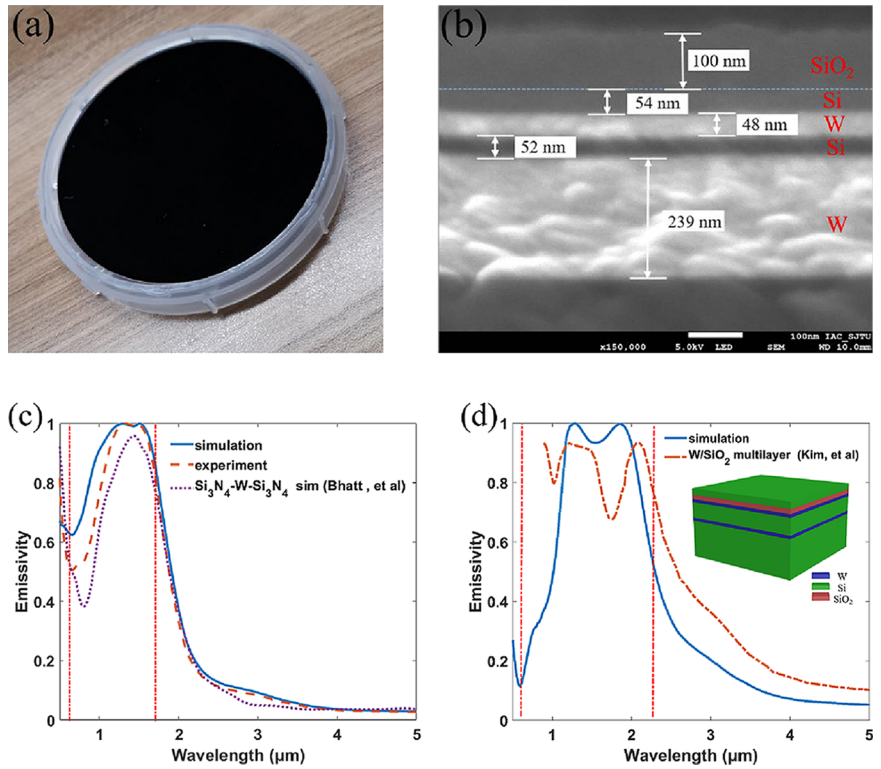

Figure 4. (a) Fabricated sample of the optimal selective TPV emitter. (b) Cross-sectional SEM image of the fabricated sample for the optimal structure. (c) Simulated emissivity of the optimal structure, the experimentally measured emissivity of the fabricated sample, and simulation results from a recent paper[52] on TPV emitters for the GsSb PV cell. (d) Simulated emissivity of the optimal structure and simulation results from ref 24 on TPV emitters for the InGaAsSb PV cell.

the optimal selective TPV emitter is 5 layers rather than 10 layers since some adjacent layers are the same material or the top layer is air. Obviously, the optimal structure is an aperiodic multilayer metamaterial which is different from the traditional periodic multilayer selective TPV emitter. As illustrated in Figure S1c,d, we have calculated all candidate structures of two random groups. As a result, the optimal structure of the selective TPV emitter obtained by the Bayesian optimization method is proved to be exactly the same as that with the largest FOM.

3.2. Fabricated Samples and Spectral Selectivity of the Optimal Selective TPV Emitter. After finding the optimal structure by Bayesian optimization, we fabricated the sample by an automatic multi-target sputtering system,[51] and the substrate is a 3 inch single throw Si wafer with a thickness of 370 μm. Figure 4a displays the sample of the optimal structure. After cutting and embedding the sample with a triple ion-beam cutter (Leica EM TIC 3X), the cross-section of the fabricated sample can be observed. Then, the cross-section scanning electron microscopy (SEM) image of the fabricated sample for the optimal structure is shown in Figure 4b by scanning with the a field-emission scanning electron microscope (FE-SEM JSM-7800F). We can see the thickness of each layer is 100, 54, 48, 52, and 239 nm from the top to the bottom. The mean square error (MSE) of the fabricating error can be defined as: $\mathrm{MSE} = \frac{1}{n}\sum_{i=1}^{n}(\mathrm{measurement}_i - \mathrm{design}_i)^2$, where n is the number of layer, and $n = 5$ for the fabricated sample of the optimal structure. Therefore, we can get the fabricating error MSE = 4. The fabricating error is mainly caused by processing errors, since the thicknesses of layers may differ due to the fabrication conditions such as the sputtering rate.

https://dx.doi.org/10.1021/acsaem.0c03201
ACS Appl. Energy Mater. 2021, 4, 2004−2013

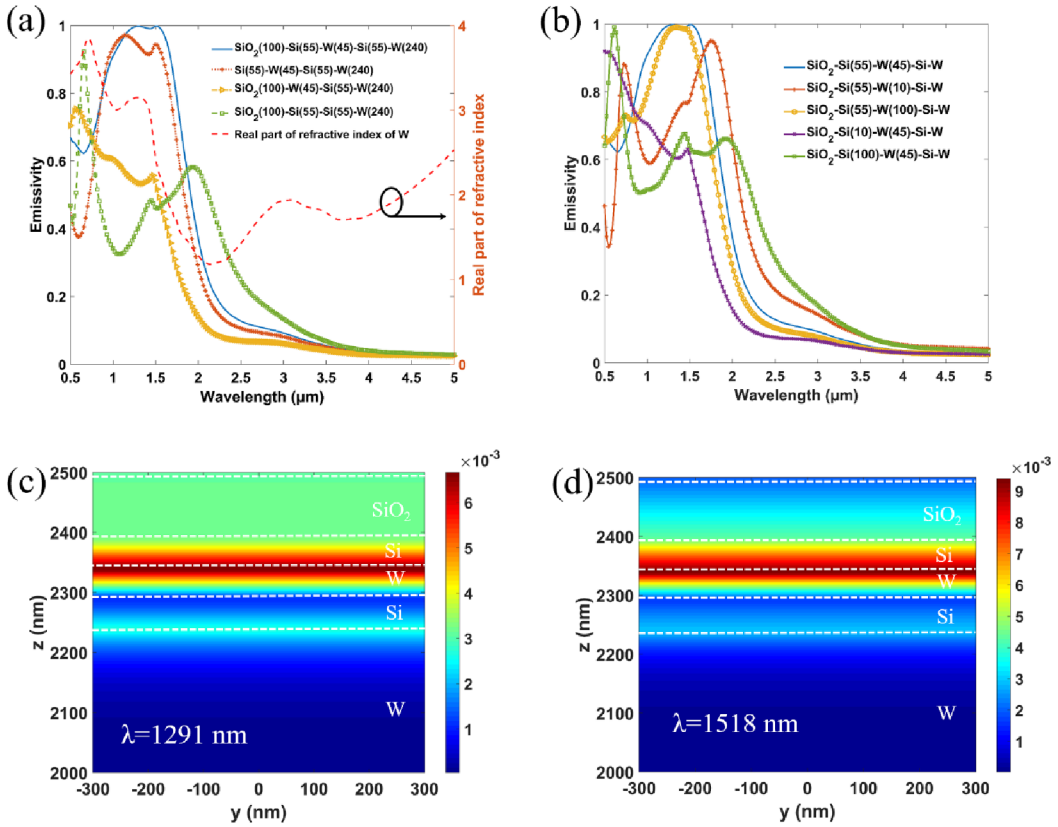

Figure 5. (a) Emission spectrum of the structures compared with the optimal structure without the SiO_2 layer, Si layer, and W layer, respectively. The red dashed line shows the real part of the refractive index of pure W. (b) Emission spectrum as a function of thickness of the W layer and Si layer of 10 nm and 100 nm, respectively. Contour plots of the magnetic field intensity at the wavelengths of (c) 1291 nm and (d) 1518 nm, respectively.

The reflectivity of the fabricated sample is recorded in the wavelength region of 500−2000 nm by using a UV/VIS/NIR spectrophotometer and in the target wavelength region of 2000−5000 nm by using Fourier-transform infrared (FTIR) spectroscopy. Therefore, the emissivity can be measured using Kirchhoff's law, i.e., $\varepsilon_\lambda = 1 - R_\lambda$. Figure 4c shows the comparison of the simulated emissivity of the optimal structure and the measured emissivity of the fabricated sample. It can be found that the simulated values are consistent with the measured values for emission spectrums. According to the measured emissivity, the optimal performance is achieved with an FOM of 81.35%. As for the slight discrepancy in the range of the short wavelength, there might be three possible reasons: the first point is that the thicknesses of each layer have a few processing errors as shown in Figure 4b. The second point is that when the thickness of each layer changes, the corresponding optical properties will change slightly. The third point is that during the fabrication process, nanostructures will be formed at the interface of the composite layer, which will affect the emission spectrum, and these nanostructures cannot be considered through the TMM. Figure 4c shows that the fabricated sample of the optimal selective TPV emitter has high emissivity that is higher than 0.98 in the broadband spectral ranges of 1.18−1.58 μm, and emissivity of the fabricated sample is lower than 0.1 at the long wavelengths above 2.58 μm. The purple dotted line in Figure 4c shows the simulated emission spectrum of the Si_3N_4-W-Si_3N_4 selective TPV emitter.[52] It is a theoretically designed three-layer structure with a fixed thickness. As can be clearly seen, the obtained optimal selective emitter has higher emissivity at the wavelength region below the band gap wavelength of the GaSb PV cell. Although some selective TPV emitters with a two-dimensional structure can further enhance the spectral selectivity, due to the complexity of fabrication, the experimental results are often unsatisfactory to the designed structures.[53,54]

In order to further verify the performance of the Bayesian optimization method, we designed new aperiodic multilayer structures by the Bayesian optimization method for the different PV cells. For instance, at 300 K, the band gap energy of the indium gallium arsenide antimonide (InGaAsSb) PV cell is 0.53 eV,[55,56] which corresponds to a band gap wavelength of 2.4 μm. We can find the maximum FOM of the optimal selective TPV emitter by Bayesian optimization, which is 78.44%, and the text flag of the optimal structure is "2 3 3 3 3 3 2 4 3 3". In the inset of Figure 4d, we can see that the materials of the optimal structure are Si/SiO_2/W/Si/W from the top to the bottom, and the thickness for each layer is 50, 35, 25, 125, and 25 nm from the top to the bottom. The total thickness of the aperiodic multilayer is 260 nm. What is more, the spectral selectivity of the optimal structure is better than the TPV emitter with the periodic multilayer structure designed by theoretical design,[24] as illustrated in Figure 4d. Therefore, we can quickly and accurately get the optimal structure corresponding to different PV cells by Bayesian optimization.

3.3. Mechanism of the Spectral Selectivity of the Optimal Selective TPV Emitter. We now discuss the mechanism of the spectral selectivity of the optimal selective

https://dx.doi.org/10.1021/acsaem.0c03201
ACS Appl. Energy Mater. 2021, 4, 2004−2013

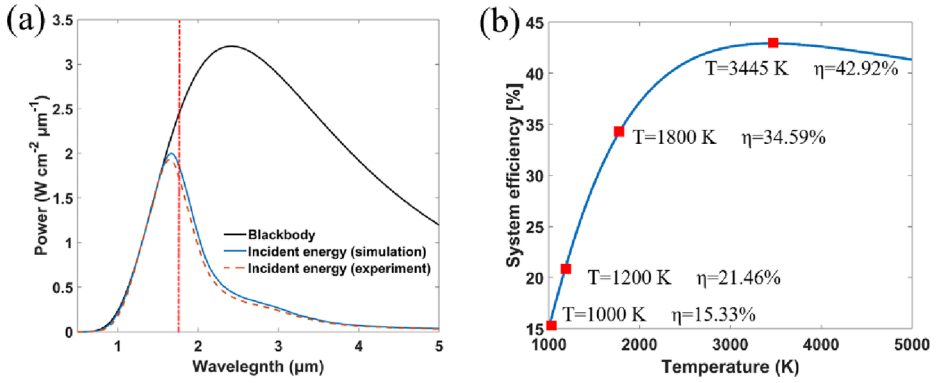

Figure 6. (a) Blackbody spectral emissive power and incident spectral energy at 1200 K. (b) TPV system efficiencies at different temperatures with ignoring the contributions from nonradiative recombination.

TPV emitter. The blue solid line in Figure 5a shows the simulated emissivity of the optimal structure of the selective TPV emitter. There are two peaks with an enhanced emissivity significantly up to about 1 at around λ = 1291 nm and λ = 1518 nm corresponding to the two peaks of the real part of the refractive index of pure W, as illustrated in Figure 5a. It can be observed that the two peaks shift to the longer wavelength due to the influence of the metal−dielectric structure. Figure 5c,d depict the contours of the magnetic field intensity at wavelengths of 1291 and 1518 nm. In the metal−dielectric structure, a strong magnetic field enhancement exists in the interface of the Si layer (the second layer) and the W layer (the third layer). The SiO_2 layer on the top acts as an antireflection layer to reduce visible and near-infrared light reflection and thereby enhance emissivity in the corresponding wavelengths. It can be seen that the emissivity of the optimal structure in the broadband spectral ranges of 1.18−1.58 μm is enhanced when the thickness of the SiO_2 layer is 100 nm compared with a structure without the SiO_2 layer (orange dotted line with pluses in Figure. 5a). What is more, the thickness of the SiO_2 layer agrees with the theory of the quarter-wave stack, as given by: $\lambda_{anti} = 4n_{anti}h_{anti}$, where n_{anti} is the refractive index of SiO_2 at λ_{anti}. Therefore, the first peak of the orange dotted line with pluses shifts to the shorter wavelength compared with the emission spectrum of the optimal structure. The yellow dashed line with triangles and the green dashed line with squares in Figure 5a are the emission spectrums of the structures compared with the optimal structure without the Si layer and W layer, respectively. It is obvious that the emission spectrums of structures without the Si layer and W layer decrease rapidly at wavelengths below the band gap wavelength of the GaSb PV cell. Therefore, the Si layer and W layer are important to the optimal structure. Figure 5b shows the effects of the thickness of the Si layer and W layer. It can be seen that the average emissivity of a spectral band from 0.6 to 1.708 μm decreases when the thickness of the Si layer is thinner at 10 nm or thicker at 100 nm. When the thickness of the W layer changes from 45 to 10 nm, the average emissivity of a spectral band from 0.6 to 1.708 μm decreases rapidly. When the thickness of the W layer changes from 45 to 100 nm, although the emissivity peaks do not show clearly preferred direction of the shifts, the spectral band of high emissivity becomes narrower. In order to make the structure of the selective TPV emitter thinner, as a result, a relatively high and broad emissivity band from 0.6 to 1.708 μm can be achieved with a thickness of the W layer around 45 nm.

3.4. TPV System Efficiency of the Optimal Selective TPV Emitter. The efficiency of the TPV system is calculated by the energy balance analysis. The incident photon energy from the experimentally measured emission spectrum of the fabricated sample is

$$P_{in} = \int_0^\infty E_{b\lambda}\varepsilon_\lambda d\lambda \tag{3}$$

In addition, the absorbed photon energy is

$$P_{abs} = \int_0^{\lambda_{bg}} \frac{\lambda}{\lambda_{bg}} E_{b\lambda}\varepsilon_\lambda \eta_{quantum,\lambda} d\lambda \tag{4}$$

where ε_λ is the measured emissivity of the fabricated sample. $\eta_{quantum,\lambda}$ denotes the EQE of the GaSb PV cell. The useful power of the PV cells can be expressed as the difference between the absorbed photon energy and the nonradiative energy loss, which can be written as:

$$P_{use} = P_{abs} - P_{loss} = P_{abs} - qVR \tag{5}$$

where q denotes the elementary charge. R denotes the nonradiative recombination rate inside the PV cell. We consider the ideal case for the TPV system, where we ignore the contributions from nonradiative recombination. Therefore, the TPV system efficiency can be calculated as $\eta = \frac{P_{use}}{P_{in}} = \frac{P_{abs}}{P_{in}}$. The blackbody spectral emissive power and incident spectral energy at 1200 K are shown in Figure 6a. The incident spectral energy calculated by the measured emissivity or simulated emissivity compared with the blackbody spectral emissive power is almost 100% when the wavelengths are less than the band gap wavelength. Note that the emissivity of the wavelengths less than 1 μm contributes little to increasing the incident spectral energy because the blackbody spectral emissive power is small in this wavelength region. Compared with the emission spectrum of the blackbody, the spectrally selective thermal emissivity can effectively suppress unwanted thermal radiation beyond the target wavelength region. According to the measured emissivity of the fabricated sample, we can obtain the efficiencies of the TPV system at different temperatures with ignoring the contributions from nonradiative recombination, as shown in Figure 6b. The maximum system efficiency is 42.92% at 3445 K. With the increase in temperature, the incident spectral energy per unit area increases and the peak value of the blackbody curve shifts to a shorter wavelength. The reason is that only photons having

https://dx.doi.org/10.1021/acsaem.0c03201
ACS Appl. Energy Mater. 2021, 4, 2004−2013

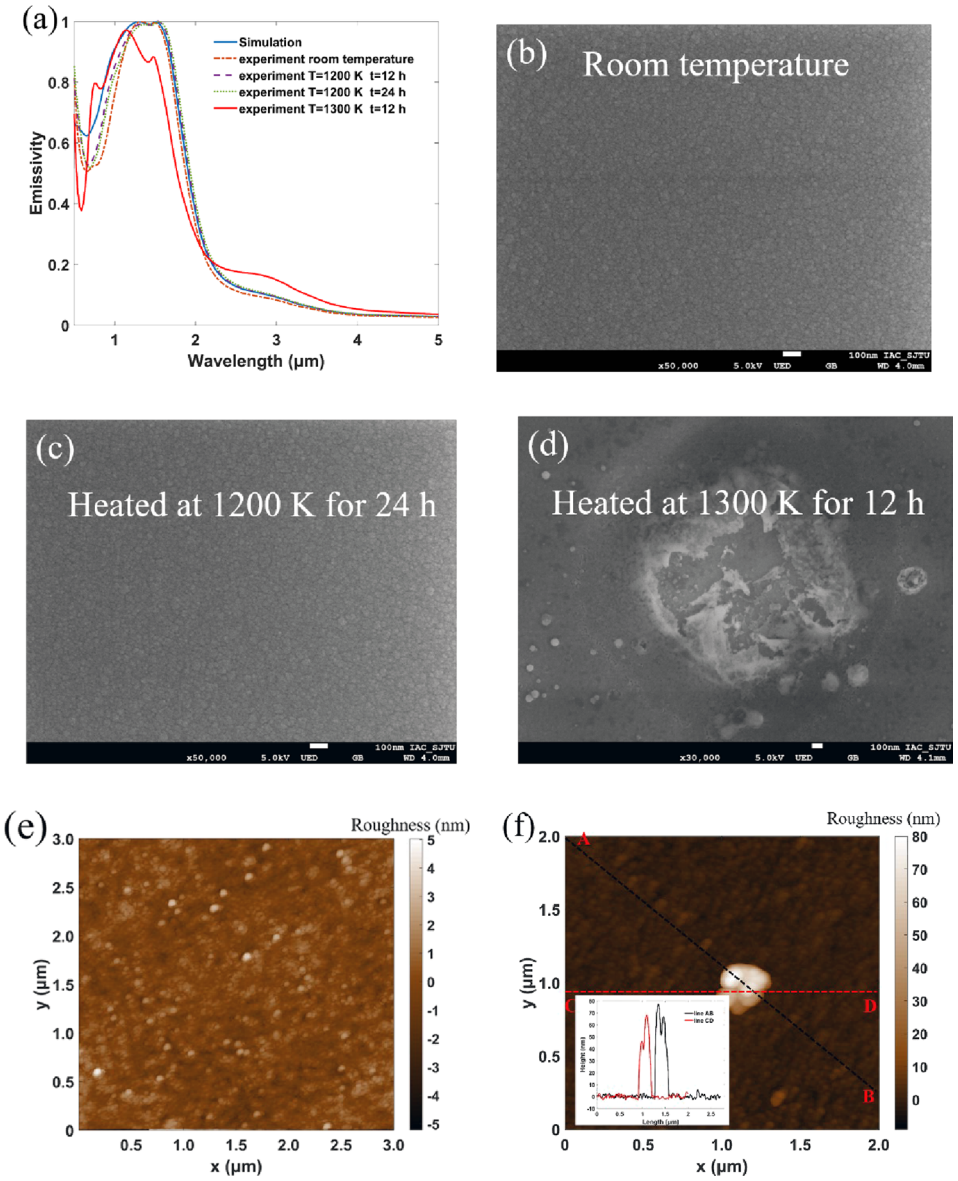

Figure 7. (a) Simulated emissivity of the optimal structure and the experimentally measured emissivity of the fabricated sample after heating at different high temperatures and times. The SEM images of the fabricated aperiodic multilayer selective TPV emitter samples: (b) before heating (room temperature); (c) after heating at 1200 K for 24 h; and (d) after heating at 1300 K for 12 h. The surface roughness of the fabricated samples characterized by AFM (e) after heating at 1200 K for 12 h and (f) after heating at 1300 K for 12 h. The inset of figure f shows the height of the sample surface with line AB and line CD.

energy above the band gap energy of the PV cell can be converted to electric energy. Therefore, as the temperature increases, we can see that the TPV system efficiency rapidly increases at the temperature lower than 3445 K. When the temperature is higher than 3445 K, the system efficiency decreases at higher temperature.

3.5. Thermal Stability and Failure Mechanisms of the Optimal Selective TPV Emitter. According to the analysis of TPV system efficiency, the efficiency is greatly affected by operating temperature of the selective TPV emitter. In order to improve and the TPV system efficiency, the long-term thermal stability of the selective TPV emitter at high operating temperature is an important factor for TPV application. We measured the emission spectrum of the fabricated samples after heating at different temperatures and times, as shown in Figure 7a. We can see that the emission spectrum of the fabricated sample after heating at 1200 K for 12 h is almost the same as the emission spectrum before heating (room temperature). What is more, when the heating time is further increased to 24 h, the emission spectrum differs only slightly. This indicates that there is good thermal stability at 1200 K, or even higher. The sample was then heated up to 1300 K, which is the highest heating temperature of a muffle furnace. We can see that the peaks of the emission spectrum have shifted and the highest emissivity becomes lower compared with the emissivity of the sample after heating at 1200 K. Figure 7b–d shows the SEM images of the top surface of the samples before heating, after heating at 1200 K for 24 h, and after heating at 1300 K for 12 h, respectively. Note that no thermal deformation of the sample after heating at 1200 K for 24 h is observed and the excellent spectral selectivity is maintained after heating. However, we can see that some damage or protrusions appear

https://dx.doi.org/10.1021/acsaem.0c03201
ACS Appl. Energy Mater. 2021, 4, 2004−2013

on the surface of the sample after heating at 1300 K for 12 h. There is an obvious damage on the sample surface, as illustrated in Figure 7d. In order to confirm the degree of destruction of these surface deformations, the surface roughness of the samples is measured by atomic force microscopy (AFM), as shown in Figure 7e,f. The surface roughness of the sample after heating at 1200 K for 12 h is less than 5 nm, which is almost the same as the sample before heating, and in the AFM image of the sample after heating at 1300 K for 12 h, we can see that the surface roughness is about 75 nm, as illustrated in Figure 7f. The inset in Figure 7f depicts the height of the sample surface, which corresponds to line AB and line CD in Figure 7f. The height is almost 75 nm in the protrusion. It means that thermal deformations mainly occur in parts of the sample surface and mainly destroy the top layer because the thickness of the SiO_2 layer is 100 nm. Although the maximum temperature of our experimental facility is limited, repeated thermal tests give a good measure of thermal stability at high temperatures. What is more, the thermal stability can be further improved by using the heat-resisting materials like silicon nitride (Si_3N_4), hafnium dioxide (HfO_2), and so on.

4. CONCLUSIONS

In this work, we use Bayesian optimization to design the highly wavelength-selective, aperiodic multilayer nanocomposite selective TPV emitters. Based on the combination of Bayesian optimization and the TMM, the design of the selective TPV emitter is optimized over 5.23×10^9 candidate structures to maximize the FOM. The maximum FOM could be realized within calculations for less than 3500 structures of each group. This means that only 0.67% of the total candidate structures needs to be calculated to determine the optimal structure, which is much better than the other machine learning algorithms. As for the GaSb PV cell, the optimized structure is an aperiodic multilayer structure with an FOM of 82.16%. The optimal structure is then fabricated, and the measured FOM is 81.35%, which is significantly higher than the structures designed and fabricated by experience. What is more, we have analyzed the theoretical efficiency of the TPV system and measured the thermal stability of the fabricated samples. The presented optimal structure of the selective TPV emitter is very encouraging and demonstrate the viability of Bayesian optimization toward obtaining a highly selective, aperiodic TPV emitter. Our results also demonstrate the possibility of automatically designing the metamaterials for specific applications via Bayesian optimization.

■ ASSOCIATED CONTENT

Supporting Information

The Supporting Information is available free of charge at https://pubs.acs.org/doi/10.1021/acsaem.0c03201.

Accuracy verification of Bayesian optimization; the number of calculated structures needed to find an optimal structure and the probability distribution of FOM obtained from traversal calculation of all the candidate structures of two random groups (Figure S1) (PDF)

■ AUTHOR INFORMATION

Corresponding Author

Changying Zhao − *Institute of Engineering Thermophysics, School of Mechanical Engineering and MOE Key Laboratory for Power Machinery and Engineering, Shanghai Jiao Tong University, Shanghai 200240, China;* orcid.org/0000-0003-0023-0378; Email: changying.zhao@sjtu.edu.cn

Authors

Wenbin Zhang − *Institute of Engineering Thermophysics, School of Mechanical Engineering and MOE Key Laboratory for Power Machinery and Engineering, Shanghai Jiao Tong University, Shanghai 200240, China*

Boxiang Wang − *Institute of Engineering Thermophysics, School of Mechanical Engineering and MOE Key Laboratory for Power Machinery and Engineering, Shanghai Jiao Tong University, Shanghai 200240, China*

Complete contact information is available at: https://pubs.acs.org/10.1021/acsaem.0c03201

Notes

The authors declare no competing financial interest.

■ ACKNOWLEDGMENTS

This work is supported by the National Natural Science Foundation of China (Grants No. 51636004, and 51906144), Shanghai Key Fundamental Research (Grants No. 18JC1413300, and 20JC1414800), Open Fund of Key Laboratory of Thermal Management and Energy Utilization of Aircraft of Ministry of Industry and Information Technology (Grant No. CEPE2020015) and the Foundation for Innovative Research Groups of the National Natural Science Foundation of China (Grant No. 51521004). The authors appreciate Dr. Shenghong Ju from China-UK Low Carbon College of Shanghai Jiao Tong University for valuable discussions on the method of Bayesian optimization.

■ REFERENCES

(1) Peris, B.; Navarro-Esbrí, J.; Molés, F. Bottoming organic Rankine cycle configurations to increase Internal Combustion Engines power output from cooling water waste heat recovery. *Appl. Therm. Eng.* **2013**, *61*, 364−371.

(2) Yu, C.; Chau, K. T. Thermoelectric automotive waste heat energy recovery using maximum power point tracking. *Energ. Convers Manage* **2009**, *50*, 1506−1512.

(3) Forman, C.; Muritala, I. K.; Pardemann, R.; Meyer, B. Estimating the global waste heat potential. *Renew. and Sust. Energ. Rev.* **2016**, *57*, 1568−1579.

(4) Campana, F.; Bianchi, M.; Branchini, L.; De Pascale, A.; Peretto, A.; Baresi, M.; Fermi, A.; Rossetti, N.; Vescovo, R. ORC waste heat recovery in European energy intensive industries: Energy and GHG savings. *Energ. Convers Manage* **2013**, *76*, 244−252.

(5) Singh, D. V.; Pedersen, E. A review of waste heat recovery technologies for maritime applications. *Energ. Convers Manage* **2016**, *111*, 315−328.

(6) Licht, A.; Pfiester, N.; DeMeo, D.; Chivers, J.; Vandervelde, T. E. A Review of Advances in Thermophotovoltaics for Power Generation and Waste Heat Harvesting. *MRS Advances* **2019**, *4*, 2271−2282.

(7) Utlu, Z.; Parali, U. Investigation of the potential of thermophotovoltaic heat recovery for the Turkish industrial sector. *Energ. Convers Manage* **2013**, *74*, 308−322.

(8) Demichelis, F.; Minetti-Mezzetti, E. A solar thermophotovoltaic converter. *Solar Cells* **1980**, *1*, 395−403.

(9) Woolf, D. N.; Kadlec, E. A.; Bethke, D.; Grine, A. D.; Nogan, J. J.; Cederberg, J. G.; Bruce Burckel, D.; Luk, T. S.; Shaner, E. A.; Hensley, J. M. High-efficiency thermophotovoltaic energy conversion enabled by a metamaterial selective emitter. *Optica* **2018**, *5*, 213−218.

(10) Pfiester, N. A.; Vandervelde, T. E. Selective emitters for thermophotovoltaic applications. *Phys. Status Solidi A* **2017**, *214*, No. 1600410.
(11) Rephaeli, E.; Fan, S. Absorber and emitter for solar thermo-photovoltaic systems to achieve efficiency exceeding the Shockley-Queisser limit. *Opt. Express* **2009**, *17*, 15145−15159.
(12) Zhou, Z.; Chen, Q.; Bermel, P. Prospects for high-performance thermophotovoltaic conversion efficiencies exceeding the Shockley−Queisser limit. *Energ. Convers Manage* **2015**, *97*, 63−69.
(13) Laroche, M.; Carminati, R.; Greffet, J.-J. Near-field thermophotovoltaic energy conversion. *J. Appl. Phys.* **2006**, *100*, No. 063704.
(14) Zhao, B.; Chen, K.; Buddhiraju, S.; Bhatt, G.; Lipson, M.; Fan, S. High-performance near-field thermophotovoltaics for waste heat recovery. *Nano Energy* **2017**, *41*, 344−350.
(15) Fiorino, A.; Zhu, L.; Thompson, D.; Mittapally, R.; Reddy, P.; Meyhofer, E. Nanogap near-field thermophotovoltaics. *Nat. Nanotechnol.* **2018**, *13*, 806−811.
(16) He, M.-J.; Qi, H.; Wang, Y.-F.; Ren, Y.-T.; Cai, W.-H.; Ruan, L.-M. Near-field radiative heat transfer in multilayered graphene system considering equilibrium temperature distribution. *Opt. Express* **2019**, *27*, A953−A966.
(17) Zhang, W. B.; Zhao, C. Y.; Wang, B. X. Enhancing near-field heat transfer between composite structures through strongly coupled surface modes. *Phys. Rev. B* **2019**, *100*, No. 075425.
(18) He, M.; Qi, H.; Ren, Y.; Zhao, Y.; Antezza, M. Active control of near-field radiative heat transfer by a graphene-gratings coating-twisting method. *Opt. Lett.* **2020**, *45*, 2914−2917.
(19) Sakakibara, R.; Stelmakh, V.; Chan, W.; Ghebrebrhan, M.; Joannopoulos, J.; Soljacic, M.; Čelanović, I. Practical emitters for thermophotovoltaics: a review. *J. Photon Energ.* **2019**, *9*, No. 032713.
(20) Lookman, T.; Alexander, F. J.; Rajan, K. *Information science for materials discovery and design*, Springer: 2016.
(21) Chirumamilla, M.; Krishnamurthy, G. V.; Knopp, K.; Krekeler, T.; Graf, M.; Jalas, D.; Ritter, M.; Störmer, M.; Petrov, A. Y.; Eich, M. Metamaterial emitter for thermophotovoltaics stable up to 1400 °C. *Sci. Rep-Uk* **2019**, *9*, 7241.
(22) Yang, Y.; Chang, J.-Y.; Sabbaghi, P.; Wang, L. Performance Analysis of a Near-Field Thermophotovoltaic Device With a Metallodielectric Selective Emitter and Electrical Contacts for the Photovoltaic Cell. *J. Heat Transfer* **2017**, *139*, No. 052701.
(23) Babiker, S. G.; Yong, S.; Sid-Ahmed, M. O.; Ming, X. Thermophotovoltaic Emitters Based on a One-Dimensional Metallic-Dielectric Multilayer Nanostructures. *J. Elect. Cooling and Therm. Control* **2014**, *04*, 10.
(24) Kim, J. H.; Jung, S. M.; Shin, M. W. High-temperature degradation of one-dimensional metallodielectric (W/SiO2) photonic crystal as selective thermal emitter for thermophotovoltaic system. *Opt. Mater.* **2017**, *72*, 45−51.
(25) Sergeant, N. P.; Pincon, O.; Agrawal, M.; Peumans, P. Design of wide-angle solar-selective absorbers using aperiodic metal-dielectric stacks. *Opt. Express* **2009**, *17*, 22800−22812.
(26) Ma, W.; Cheng, F.; Liu, Y. Deep-Learning-Enabled On-Demand Design of Chiral Metamaterials. *ACS Nano* **2018**, *12*, 6326−6334.
(27) Liu, M. Q.; Zhao, C. Y.; Wang, B. X. Design principles based on analysis in R(ε)-I(ε) space to achieve near-perfect full-spectrum volumetric solar-thermal conversion. *Sol. Energy* **2019**, *188*, 533−544.
(28) Wang, B.; Liu, M.; Huang, T.; Zhao, C. Micro/Nanostructures for Far-Field Thermal Emission Control: an Overview. *ES Energ. & Environ.* **2019**, *6*, 18−38.
(29) Kudyshev, Z. A.; Kildishev, A. V.; Shalaev, V. M.; Boltasseva, A. Machine-learning-assisted metasurface design for high-efficiency thermal emitter optimization. *Appl. Phys. Rev.* **2020**, *7*, No. 021407.
(30) Jeon, N.; Mandia, D. J.; Gray, S. K.; Foley, J. J.; Martinson, A. B. F. High-Temperature Selective Emitter Design and Materials: Titanium Aluminum Nitride Alloys for Thermophotovoltaics. *Acs Appl. Mater. Inter.* **2019**, *11*, 41347−41355.
(31) Kudyshev, Z. A.; Kildishev, A. V.; Shalaev, V. M.; Boltasseva, A. Machine learning−assisted global optimization of photonic devices. *NANO* **2020**, *10*, 371−383.
(32) Wang, H.; Alshehri, H.; Su, H.; Wang, L. Design, fabrication and optical characterizations of large-area lithography-free ultrathin multilayer selective solar coatings with excellent thermal stability in air. *Sol. Energ. Mat. Sol. C* **2018**, *174*, 445−452.
(33) Shahriari, B.; Swersky, K.; Wang, Z.; Adams, R. P.; Freitas, N. d. Taking the Human Out of the Loop: A Review of Bayesian Optimization. *P Ieee* **2016**, *104*, 148−175.
(34) Rao, J.; Ghangurde, P. Bayesian optimization in sampling finite populations. *J. Am. Stat. Assoc.* **1972**, *67*, 439−443.
(35) Qin, F.; Zhang, D.; Liu, Z.; Zhang, Q.; Xiao, J. Designing metal-dielectric nanoantenna for unidirectional scattering via Bayesian optimization. *Opt. Express* **2019**, *27*, 31075−31086.
(36) Mandt, S.; Hoffman, M. D.; Blei, D. M. Stochastic gradient descent as approximate Bayesian inference. *J. Mach. Learn. Res.* **2017**, *18*, 4873−4907.
(37) Pelikan, M.; Sastry, K.; Goldberg, D. E. Scalability of the Bayesian optimization algorithm. *Inter. J. Approx. Reason.* **2002**, *31*, 221−258.
(38) Sakurai, A.; Yada, K.; Simomura, T.; Ju, S.; Kashiwagi, M.; Okada, H.; Nagao, T.; Tsuda, K.; Shiomi, J. Ultranarrow-Band Wavelength-Selective Thermal Emission with Aperiodic Multilayered Metamaterials Designed by Bayesian Optimization. *Acs Central. Sci.* **2019**, *5*, 319−326.
(39) Bosi, M.; Pelosi, C. The potential of III-V semiconductors as terrestrial photovoltaic devices. *Progr. Photovolt.: Res. Appl.* **2007**, *15*, 51−68.
(40) Bett, A. W.; Sulima, O. V. GaSb photovoltaic cells for applications in TPV generators. *Semicond. Sci. Tech.* **2003**, *18*, S184−S190.
(41) Andreev, V. M.; Grilikhes, V. A.; Khvostikov, V. P.; Khvostikova, O. A.; Rumyantsev, V. D.; Sadchikov, N. A.; Shvarts, M. Z. Concentrator PV modules and solar cells for TPV systems. *Sol. Energ. Mat. Sol. C* **2004**, *84*, 3−17.
(42) Fraas, L. M.; Girard, G. R.; Avery, J. E.; Arau, B. A.; Sundaram, V. S.; Thompson, A. G.; Gee, J. M. GaSb booster cells for over 30% efficient solar-cell stacks. *J. Appl. Phys.* **1989**, *66*, 3866−3870.
(43) Sze, S. M.; Ng, K. K. *Physics of semiconductor devices*; John wiley & sons, 2006.
(44) Chou, J. B.; Yeng, Y. X.; Lenert, A.; Rinnerbauer, V.; Celanovic, I.; Soljačić, M.; Wang, E. N.; Kim, S.-G. Design of wide-angle selective absorbers/emitters with dielectric filled metallic photonic crystals for energy applications. *Opt. Express* **2014**, *22*, A144−A154.
(45) Zhang, Z. M. *Nano/microscale heat transfer*, Springer: 2007.
(46) Brekhovskikh, L. *Waves in layered media*; Elsevier, 2012, *16*.
(47) Palik, E. D. *Handbook of optical constants of solids*, Academic press: 1998; *3*.
(48) Ueno, T.; Rhone, T. D.; Hou, Z.; Mizoguchi, T.; Tsuda, K. COMBO: An efficient Bayesian optimization library for materials science. *Mater. Discovery* **2016**, *4*, 18−21.
(49) Shu, L.; Jiang, P.; Shao, X.; Wang, Y. A New Multi-Objective Bayesian Optimization Formulation With the Acquisition Function for Convergence and Diversity. *J. Mech. Design* **2020**, *142*, No. 091703.
(50) Guan, Q.; Alketbi, A. S.; Raza, A.; Zhang, T. Accelerated Development of Refractory Nanocomposite Solar Absorbers using Bayesian Optimization. *MRS Advances* **2020**, *5*, 1537−1545.
(51) Boyd, A. R.; O'Kane, C.; Meenan, B. J. Control of calcium phosphate thin film stoichiometry using multi-target sputter deposition. *Surf. Coat. Technol.* **2013**, *233*, 131−139.
(52) Bhatt, R.; Kravchenko, I.; Gupta, M. High-efficiency solar thermophotovoltaic system using a nanostructure-based selective emitter. *Sol Energy* **2020**, *197*, 538−545.
(53) Cui, K.; Lemaire, P.; Zhao, H.; Savas, T.; Parsons, G.; Hart, A. J. Tungsten−Carbon Nanotube Composite Photonic Crystals as Thermally Stable Spectral-Selective Absorbers and Emitters for Thermophotovoltaics. *Adv. Energy Mater.* **2018**, *8*, No. 1801471.

https://dx.doi.org/10.1021/acsaem.0c03201
ACS Appl. Energy Mater. 2021, 4, 2004−2013

(54) Kim, J.-M.; Park, K.-H.; Kim, D.-S.; Hwang, B.-Y.; Kim, S.-K.; Chae, H.-M.; Ju, B.-K.; Kim, Y.-S. Design and fabrication of spectrally selective emitter for thermophotovoltaic system by using nano-imprint lithography. *Appl. Surf. Sci.* **2018**, *429*, 138−143.
(55) Mauk, M. G.; Andreev, V. M. GaSb-related materials for TPV cells. *Semicond. Sci. Tech.* **2003**, *18*, S191−S201.
(56) Qiu, K.; Hayden, A. C. S. Direct thermal to electrical energy conversion using very low bandgap TPV cells in a gas-fired furnace system. *Energ. Convers. Manage* **2014**, *79*, 54−58.

https://dx.doi.org/10.1021/acsaem.0c03201
ACS Appl. Energy Mater. 2021, 4, 2004−2013